Nucleon form factors from N_{f}=2+1+1 twisted mass QCD at the physical point

C. Alexandrou,^{a,b} **S. Bacchio,**^{b} **M. Constantinou,**^{c} **J. Finkenrath,**^{b}
K. Hadjiyiannakou,^{a,b} **K. Jansen,**^{d} **G. Koutsou**^{b,*} **and A. Vaquero**^{e}

^{a}*Department of Physics, University of Cyprus, P.O. Box 20537, 1678 Nicosia, Cyprus*

^{b}*Computation-based Science and Technology Research Center, The Cyprus Institute, 20 Konstantinou Kavafi Str., 2121, Nicosia Cyprus*

^{c}*Temple University, 1801 N Broad Str., Philadelphia, PA 19122, USA*

^{d}*DESY-Zeuthen, 6 Platanenallee Str., 15738 Zeuthen, Germany*

^{d}*University of Utah, 201 Presidents' Cir, Salt Lake City, UT 84112, USA*

E-mail: g.koutsou@cyi.ac.cy

We present the nucleon axial and electromagnetic form factors using N_{f}=2+1+1 ensembles of twisted mass fermions with clover improvement and with masses tuned to their physical values. Excited state effects are studied using several sink-source time separations in the range 0.8 fm - 1.6 fm, exponentially increasing statistics with the separation such that statistical errors remain approximately constant. In addition, quark loop disconnected diagrams are included in order to extract the isoscalar axial form factors and the proton and neutron electromagnetic form factors, as well as their strange-quark contributions. The radii and moments are extracted by modelling the Q^2 dependence, including using the so-called z-expansion. A preliminary assessment of lattice cut-off effects is presented using two lattice spacings directly at the physical point.

**Speaker

1. Introduction

Nucleon form factors are fundamental probes of its structure, mapping for instance the charge distribution of its constituent quarks. In particular, the electromagnetic form factors determine the nucleon magnetic moment and the electric and magnetic radii, while the axial form factors probe chiral symmetry and test partial conservation of the axial current (PCAC). Electron scattering experiments can provide a precise determination of the nucleon electromagnetic form factors. Experiments, having been carried out since the fifties, are continuing at experimental facilities at Mainz and JLab. In the limit of zero momentum transfer Q^2, the slope of the electric, $G_E(Q^2)$, and magnetic, $G_M(Q^2)$, form factors is related to the electric and magnetic root mean square (rms) radii. Their value at $Q^2 = 0$ yields the electric charge and magnetic moment, respectively. Furthermore, the process $\nu_\mu + p \rightarrow \mu^+ + n$ yields the axial form factor, $G_A(Q^2)$, while the induced pseudoscalar form factor, $G_P(Q^2)$, is obtained via the longitudinal cross section in pion electro-production. The nucleon axial charge, $g_A = G_A(0)$ is measured to high precision from β-decay experiments.

In this contribution, we present a calculation of the electromagnetic and axial form factors of the nucleon using lattice QCD on three ensembles of twisted mass clover-improved fermion ensembles with quark masses tuned to yield physical pion mass values (physical point). Two ensembles are simulated with two degenerate light quarks (N_f=2), lattice spacing a=0.0937 fm and three-dimensional volumes $L^3 \simeq (4.5 \text{ fm})^3$ and $L^3 \simeq (6 \text{ fm})^3$, while the third ensemble is simulated with a strange and charm quark in addition (N_f=2+1+1), a=0.0801 fm and $L^3 \simeq (5.1 \text{ fm})^3$. The calculation of the disconnected quark loop contributions allows the extraction of the individual proton and neutron form factors, as well as the strange form factors. Furthermore, preliminary results are presented for the strange electromagnetic form factors on a physical point N_f=2+1+1 ensemble with $a \simeq 0.07$ fm and $L^3 \simeq (5.6 \text{ fm})^3$.

2. Lattice setup

2.1 Matrix elements

The form factors are obtained from the nucleon matrix elements:

$$\langle N(p', s')|O_\mu^X|N(p, s)\rangle = \sqrt{\frac{m_N^2}{E_N(\vec{p}')E_N(\vec{p})}}\bar{u}_N(p', s')\Lambda_\mu^X(q^2)u_N(p, s)$$

with $N(p, s)$ a nucleon state of momentum p and spin s, $E_N(\vec{p}) = p_0$ its energy and m_N its mass, u_N a nucleon spinor and, $q = p' - p$, the momentum transfer from initial (p) to final (p') momentum, and O^X either vector ($X = V$) or axial ($X = A$) current. The nucleon matrix element of the vector current decomposes into the Dirac F_1 and Pauli F_2 form factors, while the corresponding one of the axial current decomposes into the axial G_A and induced pseudo-scalar G_P form factors, given as

$$\Lambda_\mu^V(q^2) = \gamma_\mu F_1(q^2) + \frac{i\sigma_{\mu\nu}q^\nu}{2m_N}F_2(q^2), \quad \Lambda_\mu^A(q^2) = \frac{i}{2}\gamma_5\gamma_\mu G_A(q^2) + \frac{q_\mu\gamma_5}{2m_N}G_P(q^2). \quad (1)$$

The Dirac and Pauli form factors can also be expressed in terms of the nucleon electric G_E and magnetic G_M Sachs form factors via $G_E(q^2) = F_1(q^2) + \frac{q^2}{(2m_N)^2}F_2(q^2)$ and $G_M(q^2) = F_1(q^2) + F_2(q^2)$.

2.2 Lattice extraction of form factors

On the lattice, the required matrix elements are obtained from combinations of two- and three-point correlation functions,

$$C(\Gamma_0, \vec{p}; t_s, t_0) = \sum_{\vec{x}_s} \text{Tr} \left[\Gamma_0 \langle J_N(x_s) \bar{J}_N(x_0) \rangle \right] e^{-i(\vec{x}_s - \vec{x}_0)\cdot\vec{p}} \quad \text{and} \tag{2}$$

$$C_\mu(\Gamma_\nu, \vec{p}, \vec{p}'; t_s, t_{\text{ins}}, t_0) = \sum_{\vec{x}_{\text{ins}}, \vec{x}_s} e^{i(\vec{x}_{\text{ins}} - \vec{x}_0)\cdot\vec{q}} e^{-i(\vec{x}_s - \vec{x}_0)\cdot\vec{p}'} \text{Tr} \left[\Gamma_\nu \langle J_N(x_s) j_\mu(x_{\text{ins}}) \bar{J}_N(x_0) \rangle \right] \tag{3}$$

respectively, with J the interpolating field of the nucleon, $x_0 = (t_0, \vec{x}_0)$ the *source*, j_μ the electromagnetic or axial current, $x_{\text{ins}} = (t_{\text{ins}}, \vec{x}_{\text{ins}})$ the *insertion*, and $x_s = (t_s, \vec{x}_s)$ the *sink*. Γ_ν is a projector acting on spin indices, with $\Gamma_0 = \frac{1}{2}(1 + \gamma_0)$ and $\Gamma_k = \Gamma_0 i \gamma_5 \gamma_k$.

We form a ratio of three- to two-point functions [1] so as to cancel unknown overlaps and energy exponentials and, after taking the large time limit, yields the nucleon ground state matrix element, $\Pi_\mu(\Gamma_\nu; \vec{p}, \vec{p}')$, namely $R_\mu(\Gamma_\nu; \vec{p}, \vec{p}'; t_s; t_{\text{ins}}) \xrightarrow[t_{\text{ins}} \gg]{t_s - t_{\text{ins}} \gg} \Pi_\mu(\Gamma_\nu; \vec{p}, \vec{p}')$. Since statistical errors increase exponentially with time separation, we cannot take t_{ins} and t_s arbitrarily large and, therefore, we evaluate the convergence to the ground state using the following methods:

- *Plateau method:* We identify a time-independent window (plateau) as a function of t_{ins} and fit to extract the plate value. We seek convergence of the plateau value as we increase t_s to extract the desired matrix element.

- *Two-state fit method:* We fit the two- and three-point functions considering contributions up to the first excited state, i.e. using the expressions

$$C(\vec{p}, t_s) = \sum_{i=0}^{1} c_i(\vec{p}) e^{-E_i(\vec{p}) t_s} \quad \text{and} \tag{4}$$

$$C_\mu(\Gamma_\nu, \vec{p}, \vec{p}', t_s, t_{\text{ins}}) = \sum_{i,j=0}^{1} A_{ij}^\mu(\Gamma_\nu, \vec{p}, \vec{p}') e^{-E_i(\vec{p}')(t_s - t_{\text{ins}}) - E_j(\vec{p}) t_{\text{ins}}}, \tag{5}$$

where A_{ij}^μ are proportional to the matrix element $\langle i | O_\mu | j \rangle$, with $|0\rangle$ and $|1\rangle$ denoting the ground and first exited state and E_0 and E_1 their energies, respectively. The desired matrix element is obtained via $\Pi_\mu(\Gamma_\nu; \vec{p}, \vec{p}') = \frac{A_{00}^\mu(\Gamma_\nu, \vec{p}', \vec{p})}{\sqrt{c_0(\vec{p}') c_0(\vec{p})}}$.

- *Summation method:* we sum the ratio over t_{ins}, [2, 3] which for large t_s yields: $R_\mu^{\text{sum}}(\Gamma_\nu; \vec{p}, \vec{p}'; t_s) = \sum_{t_{\text{ins}}} R_\mu(\Gamma_\nu; \vec{p}, \vec{p}'; t_s; t_{\text{ins}}) \xrightarrow{t_s \gg} c + t_s \Pi_\mu(\Gamma_\nu; \vec{p}, \vec{p}')$. We carry out a linear fit with t_s in order to extract the desired matrix element. We will also use the *derivative summation method*, obtained by taking the finite difference of R_μ^{sum} and fitting to a constant.

For the connected three-point functions, we use sequential inversions through the sink fixing the sink momentum $\vec{p}'$ to zero, which constrains $\vec{p} = -\vec{q}$. Having $\Pi_\mu(\Gamma; \vec{q})$, different combinations of current insertion directions (μ) and projections Γ_μ yield different form factors. Using Π^V to

denote electromagnetic and Π^A for axial matrix elements, we have:

$$\Pi_0^V(\Gamma_0; \vec{q}) = C\frac{E_N + m_N}{2m_N}G_E(Q^2), \qquad \Pi_i^A(\Gamma_k; \vec{q}) = \frac{iC}{4m_N}[\frac{q_k q_i}{2m_N}G_P(Q^2) - (E_N + m_N)\delta_{ik}G_A(Q^2)],$$

$$\Pi_i^V(\Gamma_k; \vec{q}) = C\frac{\epsilon_{ijk}q_j}{2m_N}G_M(Q^2), \qquad \Pi_0^A(\Gamma_k; \vec{q}) = C\frac{-q_k}{2m_N}[G_A(Q^2) + G_P(Q^2)\frac{m_N - E_N}{2m_N}], \text{ and}$$

$$\Pi_i^V(\Gamma_0; \vec{q}) = C\frac{q_i}{2m_N}G_E(Q^2), \tag{6}$$

where $Q^2 = -q^2$, $C = \sqrt{\frac{2m_N^2}{E_N(E_N + m_N)}}$, and the projectors $\Gamma_0 = \frac{1+\gamma_0}{4}$ and $\Gamma_k = i\gamma_5\gamma_k\Gamma_0$, with $i, k = 1, 2, 3$. For the disconnected contributions, finite values of the sink momentum $\vec{p}' \neq 0$ are used to increase statistics, with details of the setup provided in Refs. [4, 5].

2.3 Lattice setup

We use two N_f=2 ensembles simulated using twisted mass clover-improved fermions and two lattice volumes as indicated in Table 1. Simulation details for these ensembles can be found in Refs. [6, 7]. Two more recent ensembles at the physical point, using N_f=2+1+1 twisted mass clover-improved fermions have also been analyzed and are shown in Table 1, with details on their simulation provided in Ref. [7].

Table 1: Bottom: details of the N_f=2 [6] and N_f=2+1+1 [7] ensembles used. Right: Statistics used for each sink-source separation for the case of the `cB211.64` ensemble.

N_f	Ens. ID	Vol.	a [fm]
2	`cA2.48`	$48^3 \times 96$	0.0937
2	`cA2.64`	$64^3 \times 128$	0.0937
2+1+1	`cB211.64`	$64^3 \times 128$	0.0801
2+1+1	`cC211.80`	$80^3 \times 160$	0.070

t_s/a	$N_{\text{src}} \times N_{\text{conf}}$ `cB211.64`
12	4×750
14	6×750
16	16×750
18	48×750
20	64×750
2-point	264×750

For the connected three-point functions, for which we use the fixed sink sequential inversion approach, we increase statistics with increasing sink-source separations, as shown in Table 1 for the case of the `cB211.64` ensemble. The multiple separations allow an analysis of excited states with the methods of Sec. 2.2 as demonstrated for an indicative example in Fig. 1.

For the disconnected quark loops, we use a combination of eigenvalue deflation [8], hierarchical probing [9], and spin and color dilution [10], as explained in Refs. [4, 5, 11]. For the connected electromagnetic form factors, we use the conserved vector current, which does not require renormalization, while for the disconnected case, we use the local vector current. The renormalization for the local vector current is carried out non-perturbatively in the RI'-MOM scheme [12] employing momentum sources, following the procedures described in Refs. [13, 14]. For the axial current, both singlet and non-singlet, are computed. For the case of the disconnected contributions, we increase statistics using additional two-point functions as indicated in the last row of the right panel of Table 1. Details regarding the methods used for obtaining the disconnected contributions can be found in Refs. [11] and [4]. For the N_f=2 ensembles, details for the separations and statistics used can be found in Refs. [15, 16].
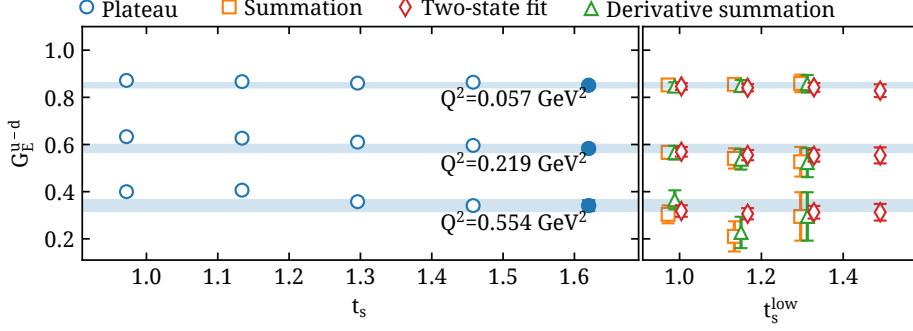
Figure 1: Plateau (circles), summation (squares), and two-state fit (rhombuses) methods used for the isovector contribution to $G_E(Q^2)$ for the cB211.64 ensemble for three values of Q^2 as indicated in the plot. t_s^{low} indicates the smallest sink-source separation used in the fit of either method. The filled symbol and band spanning the horizontal extent of the plots is chosen as the quoted value.

3. Results

3.1 Electromagnetic form factors

The proton and neutron Sachs electric ($G_E^p(Q^2)$ and $G_E^n(Q^2)$) and magnetic ($G_M^p(Q^2)$ and $G_M^n(Q^2)$) form factors are obtained in the flavor isospin limit by combining the isovector ($G_{E/M}^v(Q^2)$) and isoscalar ($G_{E/M}^s(Q^2)$) cases, via $G_{E/M}^p(Q^2) = \frac{1}{2}[G_{E/M}^v(Q^2) + \frac{1}{3}G_{E/M}^s(Q^2)]$ and $G_{E/M}^n(Q^2) = \frac{1}{2}[\frac{1}{3}G_{E/M}^s(Q^2) - G_{E/M}^v(Q^2)]$. Disconnected quark loop contributions cancel for the isovector case but need to be computed for the isoscalar case. In Fig. 2 we show results for the proton and neutron Sachs electromagnetic form factors for the two N_f=2 ensembles and the cB211.64 N_f=2+1+1 ensemble. Disconnected contributions are included in the results for the latter and the cA2.48 ensemble. Comparison between the two N_f=2 ensembles suggests that volume effects are within statistical errors for the range of volumes used here. Furthermore, our high accuracy determination of the disconnected contributions at the physical point reveals that these are at the percent level compared to connected contributions, as can be verified from Fig. 3 in which we plot them separately for the cB211.64 ensemble. In Fig. 3 we also show fits to the so-called z-expansion [17]:

$$G(Q^2) = \sum_{k=0}^{k_{\text{max}}} a_k z^k, \qquad z = \frac{\sqrt{t_{\text{cut}} + Q^2} - \sqrt{t_{\text{cut}}}}{\sqrt{t_{\text{cut}} + Q^2} + \sqrt{t_{\text{cut}}}}, \tag{7}$$

where we use $G(Q^2)$ to refer to either electric or magnetic form factor and the values for t_{cut}, the choice of k_{max} and the priors used for the fit parameters a_k are as explained in Ref. [11].

The strange electromagnetic form factors come entirely from disconnected contributions and are computed for the N_f=2+1+1 ensembles to unprecedented accuracy at the physical point. We show results in Fig. 4, where the results for the cC211.80 ensemble are preliminary. Indicatively, we note that our results are compatible recent experimental determinations by HAPPEX [18] $G_M^s(Q^2{\sim}0.62 \text{ GeV}^2) = -0.070(67)$ and by A4 [19] $G_E^s(Q^2{\sim}0.22 \text{ GeV}^2) = 0.050(38)(19)$, $G_M^s(Q^2{\sim}0.22 \text{ GeV}^2) = 0.14(11)(11)$ while our errors are at the ${\sim}25\%$ level, allowing us to connect to more accurate, upcoming determinations by Q-weak [20] experiment and MESA [21].

The magnetic form factor at Q^2=0 yields the magnetic moment $\mu_s = G_M^s(Q^2$=0), while the slope of the form factors yields the associated radii, $\langle r_{E/M}^2 \rangle^s = -6\frac{\partial}{\partial Q^2}G_{E/M}^s(Q^2)|_{Q^2=0}$. From
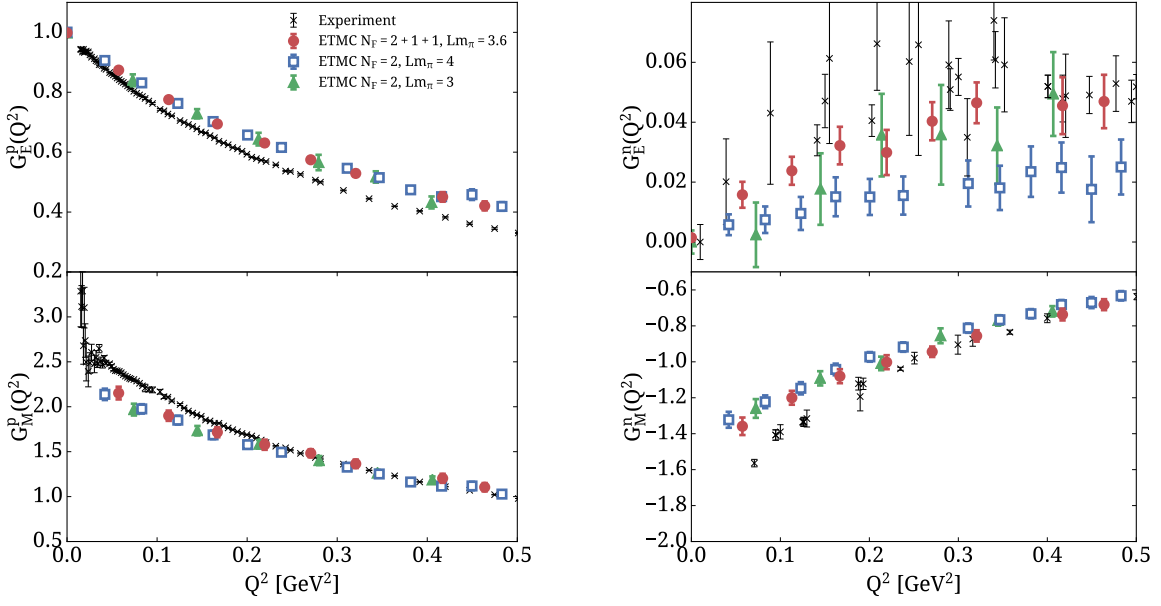
Figure 2: The proton (left) and neutron (right) electric (top) and magnetic (bottom) form factors for the two N_f=2 ensembles of Table 1 (green triangles and blue square) and for the `cB211.64` ensemble (red circles). Filled symbols indicate that disconnected contributions have been included.
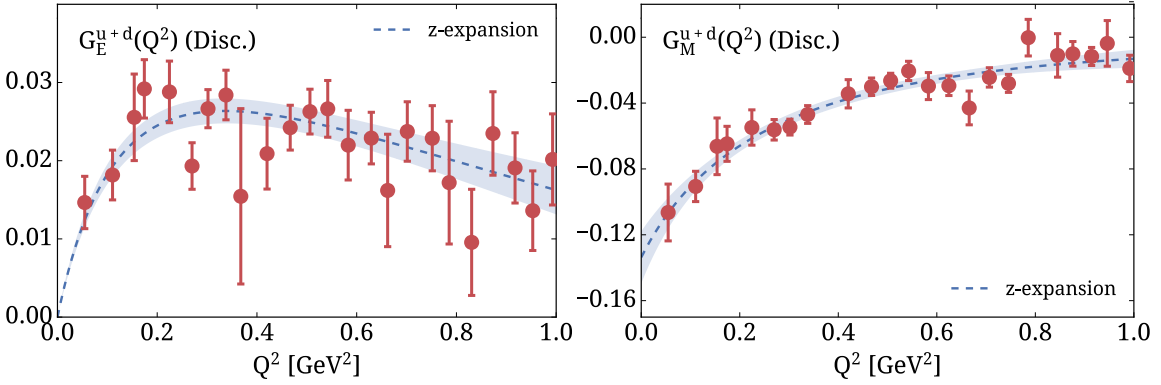

Figure 3: Disconnected contributions to the isoscalar electric (left) and magnetic (right) form factors of the nucleon for the `cB211.64` ensemble. The band is a fit to the *z*-expansion.

fits to the *z*-expansion, the radii and magnetic moment relate to the fitted parameters a_k via $\langle r^2_{E/M} \rangle^s = \frac{-3a_1^{E/M}}{2t_{\text{cut}}}$ and $\mu_s = a_0^M$, where a_k^E (a_k^M) are obtained via *z*-expansion fits to the electric (magnetic) form factors. In Fig. 5 we plot the radii and magnetic moment for the `cA2.48` and `cB211.64` ensembles and compare to other lattice QCD results. Details on the fits can be found in Ref. [4].

3.2 Axial form factors

The isovector axial form factors of the nucleon are shown for the two N_f=2 ensembles and for `cB211.64` in Fig. 6. The two N_f=2 volumes allow for a comparison of volume effects, for which do not observe any at the accuracy of out data. Furthermore, both N_f=2 ensembles with a=0.0937 fm
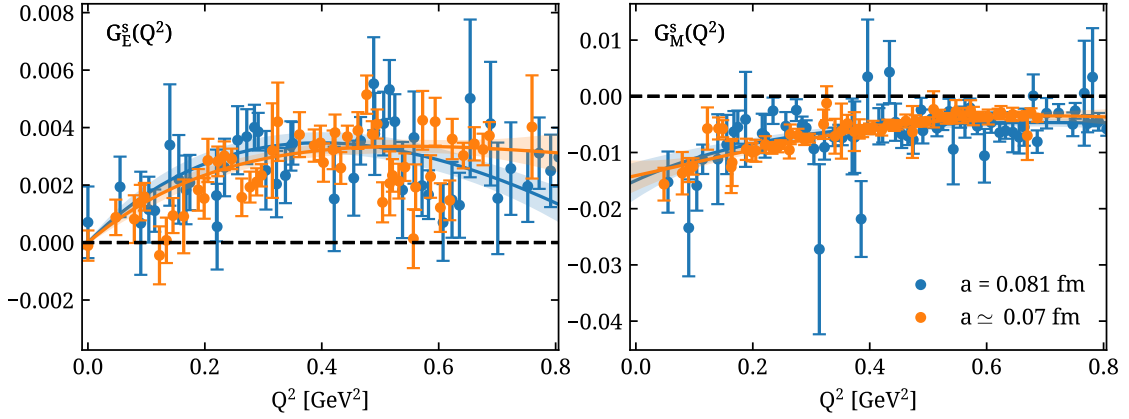
Figure 4: Strange electric (left) and magnetic (right) form factors obtained on the `cB211.64` (blue circles) and `cC211.80` (orange circles) ensembles. The curves are from fits to the *z*-expansion. Details on the results obtained for `cB211.64` can be found in Ref. [4], while results for `cC211.80` are preliminary.
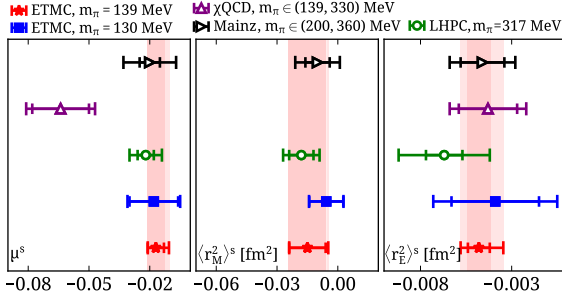

Figure 5: The nucleon strange magnetic moment (left) and magnetic (center) and electric (right) radii obtained on the `cB211.64` (red stars) and `cA2.48` (blue circles) ensembles. We compare to results from other lattice QCD calculations, namely Ref. [22] (green circles), Ref. [23] (purple triangles), and Ref. [24] (black right-pointing triangles).

are compatible with the finer N_f=2+1+1 ensemble with a=0.0801 fm. We note that the induced pseudoscalar form factor shows a large discrepancy compared to the expectation from pion pole dominance (PPD), shown with the open symbols in Fig. 7 for ensemble `cB211.64`. PPD relates the induced pseudoscalar form factor with the axial form factor, $G_P^{u-d}(Q^2) = \frac{4m_N^2}{Q^2+m_\pi^2}G_A^{u-d}(Q^2)$, where m_N and m_π are the masses of the nucleon and pion respectively and the $u-d$ superscript is used to denote that this applies for the isovector case.

In Ref. [25], it was suggested that this discrepancy may be due to excited state contamination and that the use of the temporal component of the axial current, typically unused due to its high contamination from excited states, can be fitted to identify their contribution and thus isolate, via multi-state fits, more precisely the ground state contribution. From our analysis on the `cB211.64` ensemble, shown in Fig. 7, we find that indeed the fit yields higher values of $G_P^{u-d}(Q^2)$ but not sufficient for agreement with the PPD. Further analysis is being carried out to identify other sources of systematic uncertainties, such as additional excited state contamination and cut-off effects.

In Fig. 8, we show the isoscalar and strange contributions to the nucleon axial form factor. For the isoscalar case, we plot the connected and disconnected contributions separately in addition to their sum, and observe that the disconnected contributions are negative, lowering the values obtained from the connected contributions, and significant, in contrast to the electromagnetic case. The strange axial form factor at zero momentum transfer yields the strange axial charge, for which
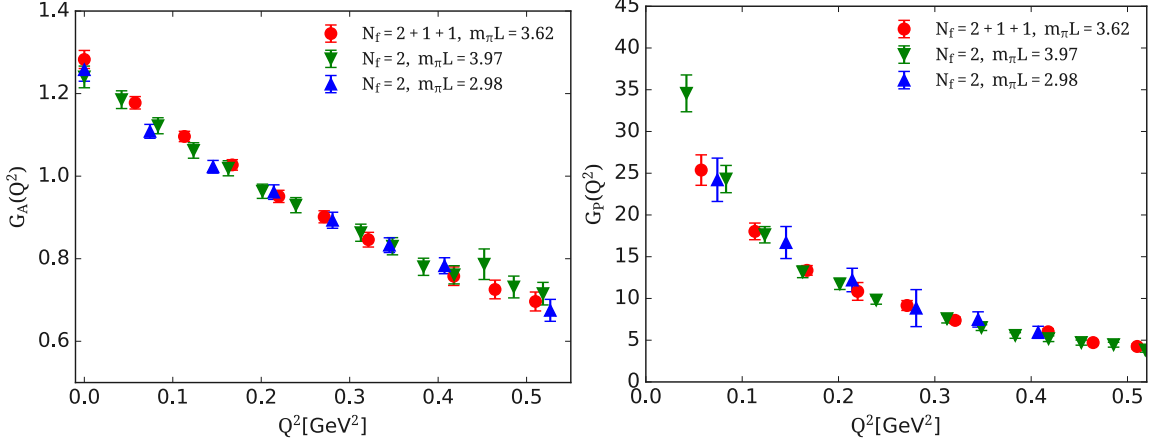
Figure 6: Isovector axial (left) and induced pseudoscalar (right) form factors of the nucleon from the `cB211.64` (red circles), `cA2.48` (blue triangles), and `cA2.64` (green down-pointing triangles) ensembles.
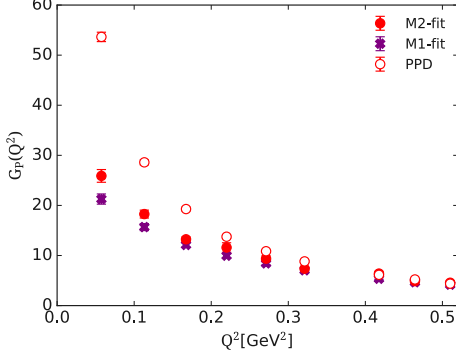

Figure 7: The induced pseudoscalar form factor, $G_P^{u-d}(Q^2)$, obtained using the lattice data for $G_A^{u-d}(Q^2)$ and PPD (open circles) as well as using two two-state fit approaches to obtain $G_P^{u-d}(Q^2)$, namely using $M1$ (crosses) in which we fit the temporal component of the axial current, i.e. Π_0^A in Eq. 6, and use the same fit parameter for E_1 in the two- and three-point function, and $M2$ (filled circles) in which we fit the same component but allowing E_1 to be different in two- and three-point function.

we find $g_A^s=G_A^s(Q^2=0)=-0.044(8)$, and is of phenomenological significance since it yields the contribution of the strange quark intrinsic spin to the nucleon spin. The bands show fits to the z-expansion, as well as to the dipole form, $G_A^s(Q^2)=G_A^s(0)/[1+\frac{Q^2}{(m_A^s)^2}]^2$. The radius is obtained from the dipole mass via $\langle r_A^2 \rangle^s = 12/(m_A^s)^2$. With the isoscalar, isovector, and strange quark contributions to the axial form factors at hand, we can construct the phenomenologically interesting SU(3) singlet $u+d+s$ and octet $u+d-2s$ combinations. The disconnected contributions to these combinations are shown in Fig. 9. We find that both combinations, for both axial and induced pseudoscalar form factors, are non-zero and negative. We note that in the SU(3) flavor symmetric limit, the octet combination should be zero, and therefore any deviation signals SU(3) flavor symmetry breaking.

The singlet and octet combinations of the nucleon axial form factor are shown in Fig. 10. The inclusion of disconnected contributions and physical point simulations is carried out for the first time for these quantities. We fit to both dipole and z-expansion forms to obtain the radii and moments. In Table 2 we tabulate results for the radii. Among z-expansion and dipole fits and the different momentum transfer cuts, we obtain consistent results within the statistical uncertainties. More details on the fits can be found in Ref. [5].
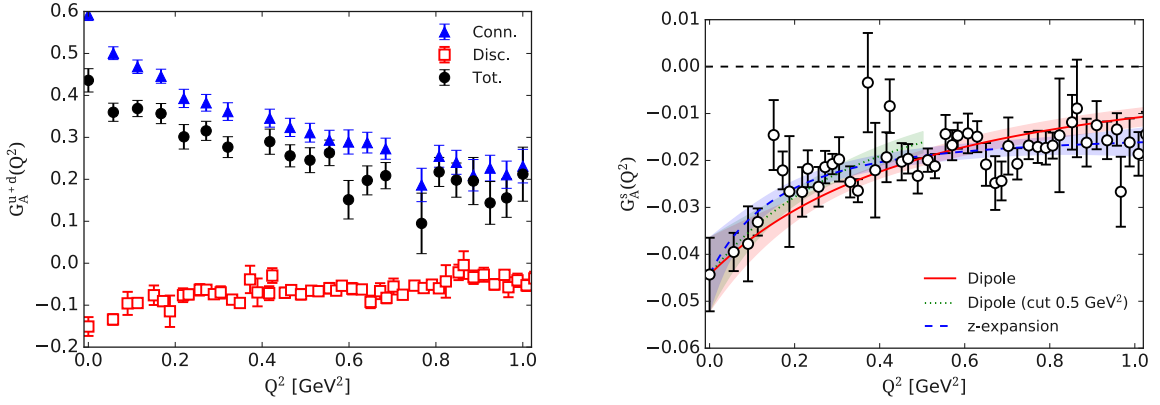
Figure 8: The isoscalar (left) and strange (right) contributions to the nucleon axial form factor. In the left panel we plot separately the connected (blue triangles) and disconnected (red squares) contributions as well as there sum (black circles). In the right panel, we also show fits to the dipole form, either fitting all data points (solid red line) or up to $Q^2 = 0.5$ GeV^2 (dotted line) as well as with the z-expansion (dashed line).
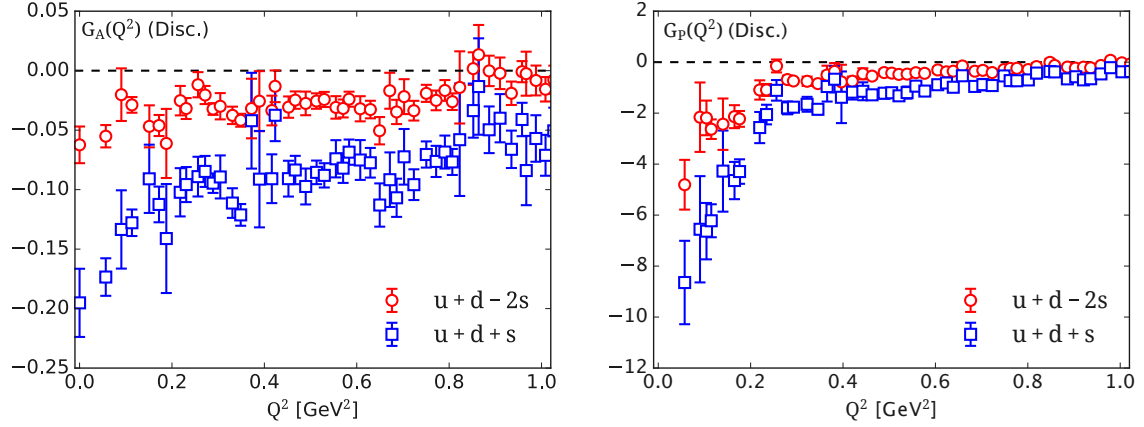

Figure 9: Disconnected contributions to the singlet (red circles) and octet (blue squares) combinations of the nucleon axial (left) and induced pseudoscalar (right) form factors for the `cB211.64` ensemble.

4. Summary and outlook

The electromagnetic and axial form factors of the nucleon are calculated using three lattice ensembles with physical pion mass at multiple sink-source separations. The two N_f=2 ensembles are simulated at two volumes and allow for studying volume effects. Our comparisons show that for the isovector case no such effects are observed within our statistics. Disconnected diagrams are calculated for an N_f=2 ensemble with a=0.0937 fm and an N_f=2+1+1 ensemble with a=0.0801 fm, which allow the determination of the proton and neutron form factors, and the strange form factors. By fitting the Q^2-dependence of these form factors we can extract phenomenological quantities of interest, such as the strange axial charge and associated radii of the nucleon. Analysis is under way using physical point N_f=2+1+1 ensembles at finer lattice spacings to evaluate cut-off effects. Preliminary results are shown here for the strange electromagnetic form factors using an ensemble with a≈0.07 fm. The additional ensembles will allow taking the continuum and infinite
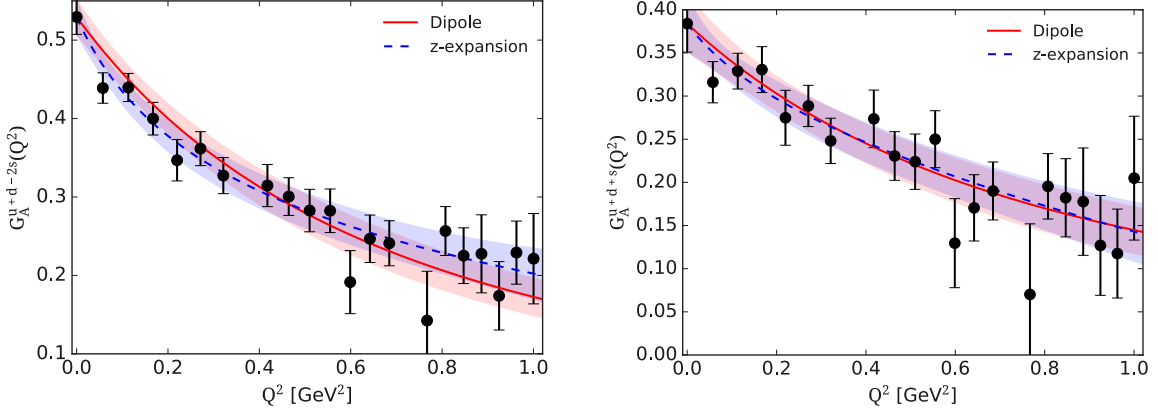
Figure 10: The singlet (left) and octet (right) combinations of the nucleon axial form factor. We show fits to the dipole (solid red curve) and *z*-expansion (dashed blue curve).

Table 2: Fit results for the axial singlet, octet, and strange radii (denoted *si*, *oc*, and *s*). We show results with a dipole or *z*-expansion form and using either data up to $Q^2 \simeq 1$ GeV^2 or $Q^2 \simeq 0.5$ GeV^2.

Fit Type	$Q^2_{\max}$ [GeV^2]	$\sqrt{\langle r_A^2 \rangle^{si}}$ [fm]	$\frac{\chi^2}{\text{d.o.f}}$	$\sqrt{\langle r_A^2 \rangle^{oc}}$ [fm]	$\frac{\chi^2}{\text{d.o.f}}$	$\sqrt{\langle r_A^2 \rangle^{s}}$ [fm]	$\frac{\chi^2}{\text{d.o.f}}$
Dipole	$\simeq 0.5$	0.623(59)	1.07	0.545(104)	0.68	0.782(145)	1.33
	$\simeq 1$	0.592(52)	1.04	0.542(81)	0.65	0.689(114)	1.48
z-expansion	$\simeq 0.5$	0.780(108)	0.45	0.673(221)	0.50	0.973(248)	0.99
	$\simeq 1$	0.761(113)	0.57	0.650(221)	0.59	0.984(239)	0.81

volume limits, while additional analyses are planned to further identify systematic errors caused by remaining excited state contamination.

Acknowledgments

References

[1] ETM collaboration, *Axial Nucleon form factors from lattice QCD*, *Phys. Rev. D* **83** (2011) 045010 [1012.0857].

[2] L. Maiani, G. Martinelli, M.L. Paciello and B. Taglienti, *Scalar Densities and Baryon Mass Differences in Lattice QCD With Wilson Fermions*, *Nucl. Phys. B* **293** (1987) 420.

[3] S. Capitani, M. Della Morte, G. von Hippel, B. Jager, A. Juttner, B. Knippschild et al., *The nucleon axial charge from lattice QCD with controlled errors*, *Phys. Rev. D* **86** (2012) 074502 [1205.0180].

[4] C. Alexandrou, S. Bacchio, M. Constantinou, J. Finkenrath, K. Hadjiyiannakou, K. Jansen et al., *Nucleon strange electromagnetic form factors*, *Phys. Rev. D* **101** (2020) 031501 [1909.10744].

[5] C. Alexandrou, S. Bacchio, M. Constantinou, K. Hadjiyiannakou, K. Jansen and G. Koutsou, *Quark flavor decomposition of the nucleon axial form factors*, *Phys. Rev. D* **104** (2021) 074503 [2106.13468].

[6] ETM collaboration, *First physics results at the physical pion mass from $N_f = 2$ Wilson twisted mass fermions at maximal twist*, *Phys. Rev. D* **95** (2017) 094515 [1507.05068].

[7] C. Alexandrou et al., *Simulating twisted mass fermions at physical light, strange and charm quark masses*, *Phys. Rev. D* **98** (2018) 054518 [1807.00495].

[8] A.S. Gambhir, A. Stathopoulos and K. Orginos, *Deflation as a Method of Variance Reduction for Estimating the Trace of a Matrix Inverse*, *SIAM J. Sci. Comput.* **39** (2017) A532 [1603.05988].

[9] A. Stathopoulos, J. Laeuchli and K. Orginos, *Hierarchical probing for estimating the trace of the matrix inverse on toroidal lattices*, 1302.4018.

[10] UKQCD collaboration, *Decay width of light quark hybrid meson from the lattice*, *Phys. Rev. D* **73** (2006) 074506 [hep-lat/0603007].

[11] C. Alexandrou, S. Bacchio, M. Constantinou, J. Finkenrath, K. Hadjiyiannakou, K. Jansen et al., *Proton and neutron electromagnetic form factors from lattice QCD*, *Phys. Rev. D* **100** (2019) 014509 [1812.10311].

[12] G. Martinelli, C. Pittori, C.T. Sachrajda, M. Testa and A. Vladikas, *A General method for nonperturbative renormalization of lattice operators*, *Nucl. Phys. B* **445** (1995) 81 [hep-lat/9411010].

[13] C. Alexandrou, M. Constantinou, T. Korzec, H. Panagopoulos and F. Stylianou, *Renormalization constants for 2-twist operators in twisted mass QCD*, *Phys. Rev. D* **83** (2011) 014503 [1006.1920].

[14] ETM collaboration, *Renormalization functions for Nf=2 and Nf=4 twisted mass fermions*, *Phys. Rev. D* **95** (2017) 034505 [1509.00213].

[15] C. Alexandrou, M. Constantinou, K. Hadjiyiannakou, K. Jansen, C. Kallidonis, G. Koutsou et al., *Nucleon electromagnetic form factors using lattice simulations at the physical point*, *Phys. Rev. D* **96** (2017) 034503 [1706.00469].

[16] C. Alexandrou, M. Constantinou, K. Hadjiyiannakou, K. Jansen, C. Kallidonis, G. Koutsou et al., *Connected and disconnected contributions to nucleon axial form factors using $N_f = 2$ twisted mass fermions at the physical point*, *EPJ Web Conf.* **175** (2018) 06003 [1807.11203].

[17] R.J. Hill and G. Paz, *Model independent extraction of the proton charge radius from electron scattering*, *Phys. Rev. D* **82** (2010) 113005 [1008.4619].

[18] HAPPEX collaboration, *New Precision Limit on the Strange Vector Form Factors of the Proton*, *Phys. Rev. Lett.* **108** (2012) 102001 [1107.0913].

[19] S. Baunack et al., *Measurement of Strange Quark Contributions to the Vector Form Factors of the Proton at Q**2=0.22 (GeV/c)**2*, *Phys. Rev. Lett.* **102** (2009) 151803 [0903.2733].

[20] D.S. Armstrong et al., *The Qweak Experiment: A Search for New Physics at the TeV Scale via a Measurement of the Proton's Weak Charge*, 1202.1255.

[21] D. Becker et al., *The P2 experiment*, *Eur. Phys. J. A* **54** (2018) 208 [1802.04759].

[22] J. Green, S. Meinel, M. Engelhardt, S. Krieg, J. Laeuchli, J. Negele et al., *High-precision calculation of the strange nucleon electromagnetic form factors*, *Phys. Rev. D* **92** (2015) 031501 [1505.01803].

[23] R.S. Sufian, Y.-B. Yang, A. Alexandru, T. Draper, J. Liang and K.-F. Liu, *Strange Quark Magnetic Moment of the Nucleon at the Physical Point*, *Phys. Rev. Lett.* **118** (2017) 042001 [1606.07075].

[24] D. Djukanovic, K. Ottnad, J. Wilhelm and H. Wittig, *Strange electromagnetic form factors of the nucleon with $N_f = 2 + 1$ $O(a)$-improved Wilson fermions*, *Phys. Rev. Lett.* **123** (2019) 212001 [1903.12566].

[25] Y.-C. Jang, R. Gupta, B. Yoon and T. Bhattacharya, *Axial Vector Form Factors from Lattice QCD that Satisfy the PCAC Relation*, *Phys. Rev. Lett.* **124** (2020) 072002 [1905.06470].